

Photodissociation dynamics of the NH molecule under intense VUV pulses

Yan Rong Liu,¹ Yong Wu,^{2,3} Jian Guo Wang,² Oriol Vendrell,⁴ Victor Kimberg^{5,6} and Song Bin Zhang^{1,*}

¹*School of Physics and Information Technology, Shaanxi Normal University, Xi'an 710119, China*

²*Institute of Applied Physics and Computational Mathematics, Beijing 100088, China*

³*Center for Applied Physics and Technology, Peking University, Beijing 100084, China*

⁴*Theoretical Chemistry, Institute of Physical Chemistry, Heidelberg University, 69120 Heidelberg, Germany*

⁵*Theoretical Chemistry and Biology, Royal Institute of Technology, Stockholm 10691, Sweden*

⁶*Siberian Federal University, 660041 Krasnoyarsk, Russia*



(Received 2 November 2020; accepted 18 November 2020; published 9 December 2020)

Photodissociation dynamics of the NH molecule excited from the triplet ground $X^3\Sigma^-$ to $2^3\Pi$ state by resonant intense VUV pulses have been comprehensively investigated by the recently proposed theoretical treatment involving the electron-rotation coupling. The rotational dynamics are described by the Wigner D functions, and the electronic transition operators are refined with respect to the changes of the projection of the total orbital angular momentum onto the molecular axis $\Delta\Lambda$. The kinetic energy release (KER) spectra and the angular distribution of photofragments are obtained by averaging over nine degenerate initial angular states, computed separately. We have shown that the KER spectra are not very sensitive to the electron-rotation coupling for different pulse intensity and energy detuning from the resonance. The angular distribution of the photofragments, on the contrary, is strongly affected by the electron-rotation coupling at the small angles between the molecular axis and laser polarization. The influence of the electron-rotational coupling shows different trends for positive and negative detunings from the resonance at variation of the pulse intensity, which is explained by sufficient changes of the rotational wave packet dynamics caused by different phases of the initial rotational states.

DOI: [10.1103/PhysRevResearch.2.043348](https://doi.org/10.1103/PhysRevResearch.2.043348)

I. INTRODUCTION

The continuous developments of ultrashort and intense laser sources, such as high-power infrared (IR) femtosecond lasers [1–3], VUV/XUV attosecond pulses [4–7], and x-ray free electron lasers (XFELs) [8–12], have advanced numerous impressive achievements in light-matter interactions in the past decades [3, 13–15]. For example, molecular field-free alignment can be efficiently obtained by impulsive intense IR lasers [16–19], pump-probe scheme and transient absorption spectroscopy developed from attosecond XUV pulses could follow the real-time electronic dynamics of atoms and electronic-nuclear dynamics of molecules with unprecedented details [3, 20, 21], and femtosecond core hole state dynamics can be tracked and beaten by ultrashort XFELs [22–27]. Among those fundamental problems, special attention was devoted to the understanding of photodissociation of diatomic molecules by intense pulses, which became an intensive area with a huge number of theoretical and experimental observations of numerous new phenomena.

Bond softening and hardening effects in the dissociation of diatomics by intense IR fields have been broadly discussed more than 20 years ago [28–31], a more favorite dressed state picture or light-induced avoided crossing can well interpret these effects [32–34]. The energy sharing between ionized electron and ion fragments from the ionization dissociation of H_2 and CO molecules by intense IR lasers have been very recently imprinted in experiments [35–38]. And the effects of light-induced conical intersections by intense VUV pulses on photodissociation have been comprehensively discussed by theory for the showcases of H_2^+ , D_2^+ , LiF , MgH^+ , Na_2 , NaI , and so on [39–49].

In our recent work [50] it was shown that for the photoexcitation and photodissociation processes by intense VUV pulses, the effects of electron-rotation coupling would play important roles on the quantities directly related to the rotational dynamics as molecular alignment and angular distribution of photofragments. A showcase for the excitation transition from singlet $X^1\Sigma$ to $^1\Pi$ states in diatomics has been comprehensively studied [50]. In contrast to the singlet diatomics with zero spin, the triplet diatomics possess spin equal to one, and its projection to the molecular axis is $0, \pm 1$. Due to this, both the electronic and spin angular moments will contribute to the photodissociation dynamics induced by the photoexcitation from state $X^3\Sigma$ to $^3\Pi$, which has to be taken into account. Moreover, one has to consider nine degenerate rotational initial states that exist for $J = 1$. This complexity results in a question: How the electron-rotation cou-

*song-bin.zhang@snnu.edu.cn

Published by the American Physical Society under the terms of the [Creative Commons Attribution 4.0 International](https://creativecommons.org/licenses/by/4.0/) license. Further distribution of this work must maintain attribution to the author(s) and the published article's title, journal citation, and DOI.

pling affects the photodissociation dynamics on triplet-triplet transition? This question is addressed and answered theoretically here, using a showcase of photodissociation dynamics in the NH molecule excited from state $X^3\Sigma^-$ to $2^3\Pi$ by intense resonant VUV pulses. We comprehensively investigated the electron-rotational coupling effects on the most common observable quantities, as kinetic energy release (KER) spectra and the angular distribution of the photofragments, with variations of the pulse intensity and the energy detuning from the resonance.

The paper is organized as follows, theoretical treatments of photodissociation for the diatomics are briefly introduced in Sec. II. Section III is devoted to the discussions of KER spectra and angular distribution of the photofragments of the

NH molecule. Conclusions of the present work are given in Sec. IV. Atomic units (a.u.) are used through the whole work unless otherwise stated explicitly.

II. COMPUTATIONAL METHODS

The time-dependent photodissociation theory has been discussed in detail in Ref. [50], here we present only an abbreviated description. Resonant excitation of an NH molecule by a linearly polarized laser field $\varepsilon(\omega, t)$ with polarization in space-fixed Z axis and the central frequency ω tuned near the resonance with the transition between the ground $X^3\Sigma^-$ and excited $2^3\Pi$ states can be described by the following nuclear Hamiltonian:

$$\mathbf{H}(\mathbf{q}, t) = \left(-\frac{1}{2m_\mu} \frac{\partial^2}{\partial q^2} + \frac{\mathbf{R}^2}{2m_\mu q^2} \right) + \begin{pmatrix} V_{3\Sigma}(q) & 0 \\ 0 & V_{3\Pi}(q) \end{pmatrix} + \begin{pmatrix} \varepsilon(\omega, t)\mu_{3\Sigma}(q)\cos\beta & (T_{3\Sigma-3\Pi})^\dagger \\ T_{3\Sigma-3\Pi} & \varepsilon(\omega, t)\mu_{3\Pi}(q)\cos\beta \end{pmatrix}, \quad (1)$$

where m_μ is the reduced mass of the NH molecule and q is the internuclear distance. \mathbf{R} is the nuclear rotational angular momentum and $\mathbf{R}^2 = \mathbf{J}^2 - \Omega^2$, with \mathbf{J} and $\Omega = \Lambda + \Sigma$ the total angular momentum and the total interior angular momentum about the molecular-fixed (MF) z axis, respectively, and Λ and Σ are the projections of the total orbital angular momentum \mathbf{L} and the spin angular moment \mathbf{S} onto the MF z axis [51]. The first term in (1) includes the vibrational and rotational kinetic operators. In the second term, $V_{3\Sigma}(q)$ and $V_{3\Pi}(q)$ correspond to the potential energy curves of the states $X^3\Sigma^-$ and $2^3\Pi$, respectively. The interactions with the laser field are described in the third term, where $\mu_{3\Sigma}(q)$ and $\mu_{3\Pi}(q)$ are the permanent dipole moments of the two electronic states, $T_{3\Sigma-3\Pi}(q)$ corresponds to the transition operator between them, and β is the Euler angle between the space-fixed (SF) Z axis and MF z axis, i.e., angle between the laser polarization and molecular axis. The geometrical meanings of various quantities as angles and angular moments are the same as in the Fig. 1 shown in the previous work [50] (not reproduced here).

In the conventional theoretical treatment, which neglects electron-rotational coupling, the angular basis functions are described by Legendre polynomials [52]:

$$|J = R, M = 0, \Omega = 0\rangle = P_J(\beta), \quad (2)$$

$$T_{3\Sigma-3\Pi} = \varepsilon(\omega, t)\mu_{3\Sigma-3\Pi}(q)\frac{\sin\beta}{\sqrt{2}},$$

where $\mu_{3\Sigma-3\Pi}(q)$ is the electronic transition dipole moment. In order to include the electron-rotation coupling (\mathbf{R} - Ω coupling), as it was done in our previous paper [50], the rotational dynamics has to be described by the L_2 -normalized Wigner D functions [52]:

$$|J, M, \Omega\rangle = \left(\frac{2J+1}{8\pi^2} \right)^{1/2} D_{M,\Omega}^J(\alpha\beta\gamma), \quad (3)$$

$$T_{3\Sigma-3\Pi} = \varepsilon(\omega, t)\mu_{3\Sigma-3\Pi}(q)\frac{\sin\beta}{\sqrt{2}} e^{i\gamma},$$

for $\Delta\Lambda_{3\Sigma-3\Pi} = 1$. Here α and γ are the Euler angles representing rotations around the SF Z axis and MF z axis,

respectively [53]. The time-dependent nuclear dynamic equation is

$$i\frac{\partial}{\partial t}[\Phi_{3\Sigma}, \Phi_{3\Pi}]^T = \mathbf{H}(q, t)[\Phi_{3\Sigma}, \Phi_{3\Pi}]^T, \quad (4)$$

which can be numerically solved by the multiconfiguration time-dependent Hartree (MCTDH) method with a specific initial condition [52].

Within the time-dependent frame, the kinetic energy release (KER) spectra and angular distribution of the photofragment can be calculated by the technique of complex absorbing potential (CAP) with the form of $-iW(q) = -i\eta(q - q_c)^3\Theta(q - q_c)$, where η is the CAP strength, q_c is the point where the CAP is switched on, and Θ is Heaviside's step function. The dissociated angular distribution in the upper

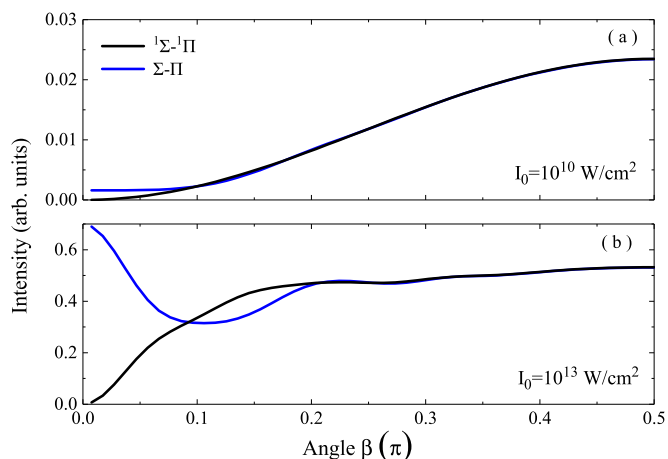


FIG. 1. Angular distributions of the MgH^+ photofragments dissociating on state 1Π excited from $1\Sigma^+$ by an 80 fs resonant pulse for the weak 10^{10} W/cm^2 (a) and strong 10^{13} W/cm^2 (b) field intensities. Results by $1\Sigma^-1\Pi$ (black lines) and $\Sigma-\Pi$ (blue lines) indicate calculations with and without \mathbf{R} - Ω coupling, respectively.

state $^3\Pi$ is calculated according to the following formula [52]:

$$P_{\text{angle}}(\beta_j) = \frac{1}{w_j} \int_0^\infty \langle \Phi_{^3\Pi}(t) | W_{\beta_j} | \Phi_{^3\Pi}(t) \rangle dt, \quad (5)$$

where w_j is the weight factor corresponding to the relevant grid point in the applied DVR basis, and W_{β_j} is the projection of the CAP on a specific grid point associated with the rotational degree of freedom [43]. The KER spectra is given by [52]

$$P_{\text{KER}}(E) = \frac{1}{\pi} \int_0^\infty \int_0^\infty \langle \Phi_{^3\Pi}(t) | W | \Phi_{^3\Pi}(t') \rangle e^{-iE(t-t')} dt dt', \quad (6)$$

where W is the CAP applied at the grid space related to the vibrational degree of freedom [43]. Note that $P_{\text{angle}}(\beta)$ and $P_{\text{KER}}(E)$ indicate the angular distributions and energy spectra integrating over energies and angles, respectively. $\int P_{\text{angle}}(\beta) d\beta = \int P_{\text{KER}}(E) dE$ is the total ion yield.

Before presenting the results of NH molecule, let us briefly discuss the angular distribution of the photofragments of the well studied MgH^+ singlet system excited from the $^1\Sigma^+$ to $^1\Pi$ state by an 80 fs resonant intense pump pulse, which is recomputed here by taking into account the $\mathbf{R}\text{-}\Omega$ coupling. The same molecular parameters and numbers of basis sets as Ref. [45] are used in the calculations. Figure 1 compares the angular distributions of MgH^+ photofragments when $\mathbf{R}\text{-}\Omega$ coupling is included (labeled by $^1\Sigma\text{-}^1\Pi$, the present improved method) and neglected (labeled by $\Sigma\text{-}\Pi$, the conventional method employed in [45]). The results of $\Sigma\text{-}\Pi$ totally reproduce the ones of Ref. [45], while the $\mathbf{R}\text{-}\Omega$ coupling changes the profile drastically. This effect has been comprehensively discussed in our previous work for a general model of the bound-dissociative transition [50]. The $\mathbf{R}\text{-}\Omega$ coupling brings very important rotational dynamics for the molecules in intense fields.

Contrary to the singlet MgH^+ system with zero total spin, the NH system is in the triplet state, and both spin and electronic angular momentum contribute to the interior angular momentum as $\Omega = \Sigma + \Lambda$ for the excited state $2^3\Pi$, and the number of initial degenerate angular states for $X^3\Sigma^-$ is nine. To study the effects of $\mathbf{R}\text{-}\Omega$ coupling in a much more complex system, we use potential energy curves and transition dipole moments taken from Ref. [54] (see Fig. 2). Besides the resonant excitation, we also considered positive and negative detuning from the resonance with the $X^3\Sigma^-$ to $2^3\Pi$ transition, marked as A, B, and C in Fig. 2(a), respectively. The effects of the field intensity is also studied. The results are obtained for the common physical observable quantities as KER spectra and angular distribution of photofragments will be studied.

The simulations are implemented with the Heidelberg MCTDH package [55]. The driving lasers are simulated by the sin-square pulse $[\sin^2(\frac{\pi t}{T})]$ with $T = 80$ fs and varied pulse intensities. The vibrational degree of freedom (DOF) q is described by 389 sin-DVRs equally distributed in the region of [1.2–40.0] a.u.; 101 basis functions have been used for the rotational DOF β by Legendre polynomials in the conventional treatment and L_2 -normalized Wigner D functions in the improved treatment, 11 and 5 exp-DVR for γ

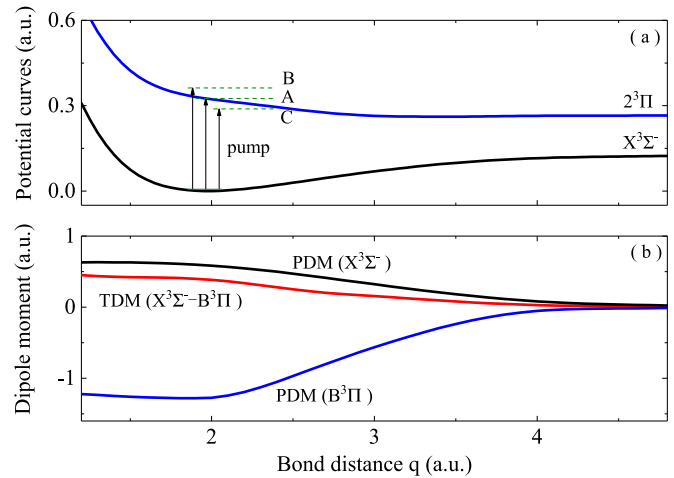


FIG. 2. (a) Potential energy curves of the NH molecule for the ground $X^3\Sigma^-$ (black line) and excited $2^3\Pi$ (blue line) electronic states; points A, B, and C label resonant energy ($\omega = 8.68$ eV), and positive ($\omega = 9.68$ eV) and negative ($\omega = 7.68$ eV) detunings from the resonance, respectively. (b) Permanent dipole moment (PDM) for the states $X^3\Sigma^-$ (black line) and $B^3\Pi$ (blue line), and transition dipole moment (TDM) between $X^3\Sigma^-$ and $2^3\Pi$ (red line), reproduced from Ref. [54].

and α , respectively. The number of single particle functions for both DOF on the two electronic states was 10. The CAP is applied with $\eta = 5 \times 10^{-5}$ a.u. and $q_c = 30$ a.u. Supposing the molecular rotational temperature is quite low, for the initial electronic state $^3\Sigma$, its nine degenerate initial angular states $|J_{^3\Sigma}^0 = 1, M_{^3\Sigma} = (0, \pm 1), \Omega_{^3\Sigma} = \Sigma_{^3\Sigma} = (0, \pm 1)\rangle$ are considered. In the rest of the article, results of $\Sigma\text{-}\Pi$ represent conventional theoretical treatment, and $^3\Sigma\text{-}^3\Pi$ indicates the improved theoretical treatment including $\mathbf{R}\text{-}\Omega$ coupling from both the spin and orbital angular momentum.

III. RESULTS AND DISCUSSIONS

A. Resonant pump in weak fields

For the description of the NH molecule excitation on $X^3\Sigma^-$ to $2^3\Pi$ transition by a weak resonant ($\omega = 8.68$ eV) pulse, first order perturbation theory can be applied. The transition strength from the rovibronic dynamics can be described as an average value of the transition operator

$$T_{J_0} = \sum_{\nu' J'} |\langle J', M_0, \Omega'; \nu'(J') | T_{^3\Sigma\text{-}^3\Pi}(\omega) | \nu(J_0); J_0, M_0, \Omega_0 \rangle|^2, \quad (7)$$

where the subscript 0 indicates the initial state, and $|\nu(J)\rangle$ indicates the ν th vibrational wave function of rotational quantum state J . For weak transitions only limited rotational states are excited, the splitting of rotational levels is quite small as compared to the vibrational states, both the energy levels and wave functions of vibrational states could be well supposed to be independent on J . It could be a proper approximation to separate the transition strength into vibrational and rotational parts as $T_{J_0} \simeq T^V T_{J_0}^R \propto T_{J_0}^R$, with the vibrational term $T^V = \sum_{\nu'} |\langle \nu' | \mu_{^3\Sigma\text{-}^3\Pi}(\omega) | \nu \rangle|^2$ and the rotational term $T_{J_0}^R$, which

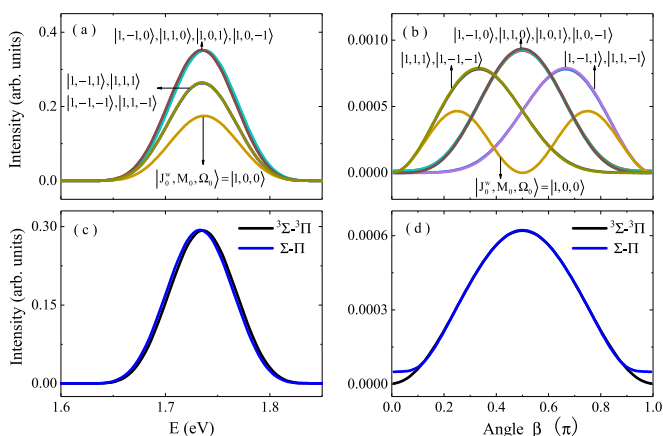


FIG. 3. KER spectra (a) and angular distribution (b) of the NH photofragments dissociating on state $2^3\Pi$ excited by a weak resonant pump laser in the $^3\Sigma^-3\Pi$ model for a different initial angular state $|J_0^w, M_0, \Omega_0\rangle$. KER spectra (c) and angular distribution (d) by treatments $^3\Sigma^-3\Pi$ (black lines) and $\Sigma-\Pi$ (blue lines).

can be expressed for the treatment without $\mathbf{R}-\Omega$ coupling ($\Sigma-\Pi$) as

$$T_{J_0}^R = \sum_{J_j^p} \left| \left\langle J_j^p, 0, 0 \left| \frac{\sin\beta}{\sqrt{2}} \right| J_0^p, 0, 0 \right\rangle \right|^2, \quad (8)$$

and for the case when $\mathbf{R}-\Omega$ coupling included ($^3\Sigma^-3\Pi$) as

$$T_{J_0^w M_0 \Omega_0}^R = \sum_{J_j^p} \left| \left\langle J_j^p, M_0, \Omega_0 + 1 \left| \frac{\sin\beta}{\sqrt{2}} e^{i\gamma} \right| J_0^w, M_0, \Omega_0 \right\rangle \right|^2. \quad (9)$$

For the initial electronic state $X^3\Sigma^-$, in the $\Sigma-\Pi$ treatment $J_0^p = 0$ and $\sin\beta$ function selects all even integers for J_j^p , so we can easily get $T_{J_0^p=0}^R = \frac{1}{3}$. In the full $^3\Sigma^-3\Pi$ treatment $J_0^w = 1$, $M_0 = (0, \pm 1)$, and $\Omega_0 = \Sigma_0 = (0, \pm 1)$, the increasing of Ω by one in the excited state comes from the selection of $e^{i\gamma}$ by $\Delta\Lambda = 1$, J_j^w could be 0, 1, and 2 from the selection of $\sin\beta$ and initial quantum numbers. As a result, there are nine degenerate initial rotational states. The total $T_{J_0^w}^R$ can be computed by the averaging over all the initial rotational states as $T_{J_0^w=1}^R = \frac{1}{9} \sum_{M_0, \Omega_0} T_{J_0^w=1, M_0, \Omega_0}^R = \frac{1}{3} = T_{J_0^p=0}^R$. This analysis shows that in the perturbation region, both treatments predict the same excitation intensity, so the effect of the electron-rotational coupling is absent.

Figures 3(a) and 3(c) show the initial rotational state resolved (for each of the nine states) and averaged KER spectra in the $^3\Sigma^-3\Pi$ model, respectively, for the case of a weak resonant pulse intensity $I_0 = 10^{10}$ W/cm². The maxima of all individual spectra are located around energy 1.73 eV and are grouped in three spectral intensity classes with ratios of about 2 : 3 : 4. This is totally consistent with the transition strength from different initial degenerate rotational states: $T_{100}^R : (T_{111}^R = T_{1-1-1}^R = T_{11-1}^R = T_{1-11}^R) : (T_{1-10}^R = T_{110}^R = T_{101}^R = T_{10-1}^R) = 2 : 3 : 4$. The correspondent angular distribution of the photofragments are shown in Figs. 3(b) and 3(d). As it shows, a different initial rotational state results in

four different profiles of the angular distribution function: an initial rotational state $|1, 0, 0\rangle$ contributes two peaks located at $\beta \approx 0.25\pi$ and 0.75π symmetric to $\beta = \pi/2$ point, $|1, 1, 1\rangle$ and $|1, -1, -1\rangle$ initial states contribute with a peak at $\beta \approx 0.35\pi$, and the symmetric peak at $\beta \approx 0.65\pi$ comes from $|1, -1, 1\rangle$ and $|1, 1, -1\rangle$ initial states, and the rest of the states contribute to the peak at $\beta = \pi/2$. The ratio for the total yield of fragments from different initial states is consistent with that of transition strength $T_{J_0^w M_0 \Omega_0}^R$. The total averaged spectra keep the nice \sin^2 -like profile with the maximum position at $\beta = \pi/2$.

The blue lines in Figs. 3(c) and 3(d) show the KER spectra and angular distribution of the photofragments in the weak field by the approach neglecting electron-rotational coupling. Since in first order perturbation regime the transition strength $T_{J_0^p=0}^R$ equals to $T_{J_0^p=1}^R$, the total yield of photofragments is almost the same for both treatments as expected, so do the profiles of KER spectra and angular distributed photofragments. Note that the slight shift of 0.004 eV to the higher energy region of KER spectra [Fig. 3(c)] computed with $\mathbf{R}-\Omega$ coupling included comes from the difference in the initial energy level of $J_0^w = 1$ and $J_0^p = 0$ rotational states in the $^3\Sigma^-3\Pi$ and $\Sigma-\Pi$ models, respectively. In the treatment by Legendre polynomials ($\Sigma-\Pi$ model), the angular distributed photofragments also slightly deviate from the \sin^2 -like profile at small angles [Fig. 3(d)], which indicates that the separation of T_{J_0} into two independent parts (rotational and vibrational contributions) is not fully applicable. Indeed, since all even values of J_j^p will be excited, excitations with higher rotational levels deviate more and more from the cases of resonant excitation, resulting in the non-negligible dependence of T^V on the rotational states. Note that if T^V was totally independent on J_0 , the angular distribution of fragments should totally follow the profile of \sin^2 . While in the treatment of Wigner D functions ($^3\Sigma^-3\Pi$ model), J_j^w could be 0, 1, and 2, the energy levels lifted by rotations are quite small, T^V depends weakly on J_0 . For strong field excitations as shown below, intense rovibrational dynamics will result in quite different spectra.

B. Resonant pump in intense fields

Figure 4 shows the fragment KER spectra and angular distributions of NH excited by resonant pulses with intensities $I_0 = 10^{13}$ [Figs. 4(a) and 4(b)], 10^{14} [Figs. 4(c) and 4(d)], and 4×10^{14} [Figs. 4(e) and 4(f)] W/cm². As it shows, increasing of the pulse intensity broaden the KER spectra, and both treatments predict quite similar KER profiles, besides a small shift due to different energy positions of the initial level, as discussed in Fig. 3(c). Indeed, the KER spectra are not directly related to the molecular rotational dynamics, and its profile shows weak sensitivity to the $\mathbf{R}-\Omega$ coupling. The spreading and splitting of KER spectra are general properties of spectra in strong field [56]. With higher rotational states excited in intense field, the case of resonant excitation in weak field turns into a negatively detuned excitation in strong field; as in the dressed picture introduced in Ref. [57], the transition between the positively dressed state of $X^3\Sigma^-$ and the negatively dressed state of $2^3\Pi$ would dominate the excitation by the negatively detuned pulse, resulting in the gradual shifting

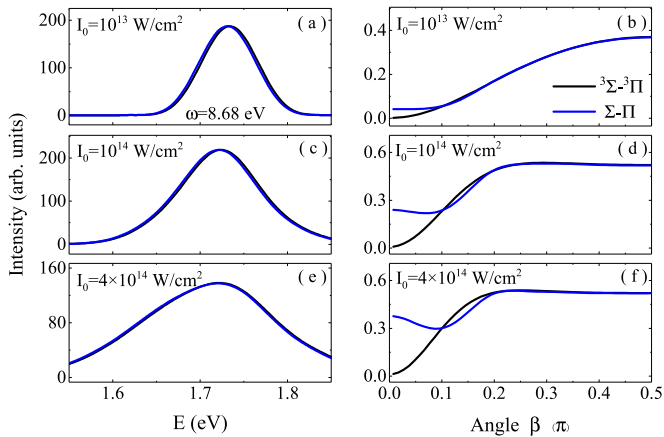


FIG. 4. KER spectra [left, panels (a, c, e)] and angular distribution [right, panels (b, d, f)] of the NH photofragments by resonant excitation computed in the ${}^3\Sigma\text{-}{}^3\Pi$ (black lines) and $\Sigma\text{-}\Pi$ models (blue lines). Three different pulse intensities are shown: 10^{13} W/cm 2 [upper panels (a, b)], 10^{14} W/cm 2 [middle panels (c, d)], and 4×10^{14} W/cm 2 [lower panels (e, f)].

of peak position to the lower energy region with the increasing of I_0 as revealed in Fig. 4. Surely we would expect the opposite variations of peak positions in the positively detuned transitions, as verified in the next subsection.

For the fragment angular distributions, the $\mathbf{R}\text{-}\Omega$ coupling results in totally different distributions at small angles. The intensity tends to zero at small β in the full ${}^3\Sigma\text{-}{}^3\Pi$ model, mistakenly turned into a very significant value in the approximate $\Sigma\text{-}\Pi$ model (Fig. 4, right). For example, the ratios between intensities around $\beta = 0$ and $\pi/2$ have increased from 8% to 72% with $I_0 = 10^{13}$ to 4×10^{14} W/cm 2 in the model of $\Sigma\text{-}\Pi$, such ratios are ~ 0 in the model of ${}^3\Sigma\text{-}{}^3\Pi$, indicating the importance of including the $\mathbf{R}\text{-}\Omega$ coupling, similar features have been comprehensively discussed in our previous work [50]. Furthermore, a broad plateau around $\beta = \pi/2$ gradually appears, predicted by both treatments, the region of the plateau has increased from $[\sim 0.45\pi, 0.5\pi]$ to $[\sim 0.2\pi, 0.5\pi]$ with $I_0 = 10^{13}$ to 4×10^{14} W/cm 2 .

For deeper understanding of the angular distribution function, let us consider the angular distributions of the individual initial rotational states, computed in the $\mathbf{R}\text{-}\Omega$ coupling model, presented in Fig. 5 for $I_0 = 10^{13}$ and 4×10^{14} W/cm 2 . As it shows, for intense pulses the relative intensities for $|J_0^w, M_0, \Omega_0\rangle = |1, 0, 0\rangle$, $|1, 1, 1\rangle$, and $|1, -1, -1\rangle$ (or $|1, -1, 1\rangle$ and $|1, 1, -1\rangle$) increase and shift to the lower (higher) angle region, which contributes the platform and its broadening revealed in Fig. 4. Note that for very intense pulse of $I_0 = 4 \times 10^{14}$ W/cm 2 , the spectra intensity around $\beta = 0$ (or π) for $|J_0^w, M_0, \Omega_0\rangle = |1, 0, -1\rangle$ and $|1, 1, 0\rangle$ (or $|1, 0, -1\rangle$ and $|1, -1, 0\rangle$) are not tiny any more, due to the excitations to higher rotational states by the intense pulse and T^V depends on higher rotational states, furthermore, there is also the coincidence for the upper states when $\Omega = M$ (or $-M$), the angular function $|D_{M,\Omega}^J(\alpha\beta\gamma)|^2$ is not zero at $\beta = 0$ (or π). For much stronger pulses, the distributions around $\beta = 0$ (or π) could be significant and must be contributed

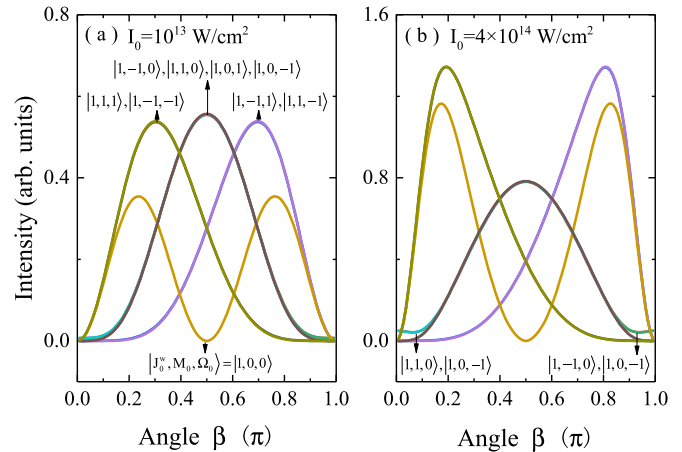


FIG. 5. Angular distribution of nine different initial angular states $|J_0^w, M_0, \Omega_0\rangle$ for two different pulse intensities: $I_0 = 10^{13}$ (a) and 4×10^{14} (b) W/cm 2 .

from initial rotational states of $|J_0^w, M_0, \Omega_0\rangle = |1, 0, -1\rangle$ and $|1, 1, 0\rangle$ (or $|1, 0, -1\rangle$ and $|1, -1, 0\rangle$).

C. Role of the detuning from the resonance

Two cases of nonresonant pump with central frequency $\omega = 9.68$ and 7.68 eV, detuned from the resonance by 1.0 and -1.0 eV, respectively, for different intensities are presented in Figs. 6 and 7, respectively. The KER spectra show a very minor effect of the $\mathbf{R}\text{-}\Omega$ coupling. Similar to the resonant pump case both treatments predict a nearly equivalent KER profile except for the discussed above little shift due to the lifting of the initial rotational state energy, and the KER spectra broaden with the increase of pulse intensities. The most sufficient effect of the electron-rotational coupling is found for the case of positive detuning at highest pulse intensity $I_0 = 4 \times 10^{14}$ W/cm 2 . With increasing of I_0 the peak position shifts to the lower and higher energy region for the negative and positive detuning, respectively, which is consistent with the dressed picture interpreted in the last subsection or Ref. [57].

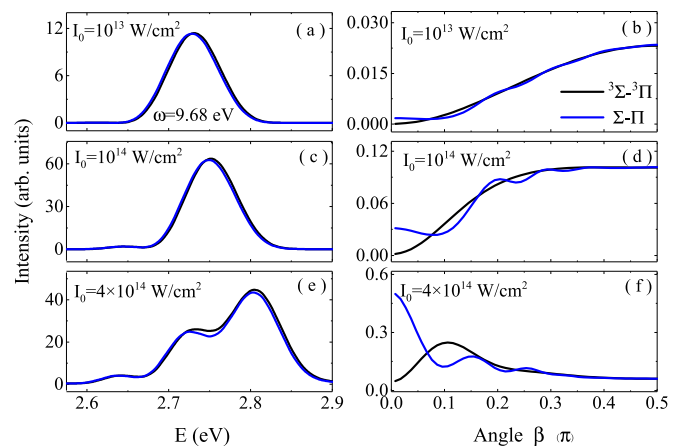


FIG. 6. Same as Fig. 4 but with positive detuning of the pump pulse with $\omega = 9.68$ eV.

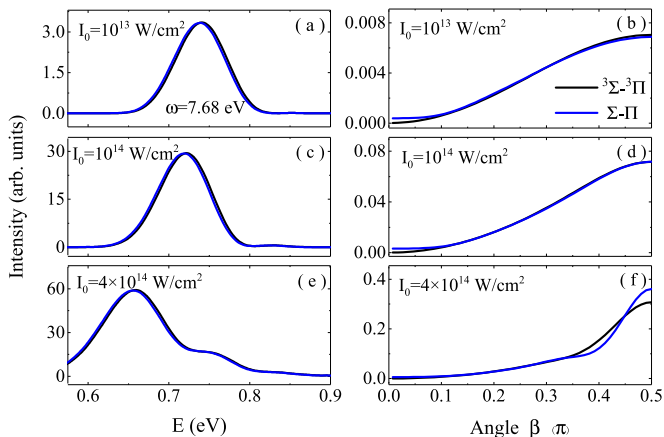


FIG. 7. Same as Fig. 4 but with negatively detuning of the pump pulse with $\omega = 7.68$ eV.

For the angular distribution of photofragments, both treatments show that the spectra exhibit more significant variations with respect to I_0 for the case of positive detuning of the pumping field. As revealed in Fig. 6, with increasing of pulse intensity, the spectra shows oscillation structures in the model without $\mathbf{R}\text{-}\Omega$ coupling included, which is quite different from that of the resonant pump case, indicating more intense rotational dynamics; the spectra in the model of ${}^3\Sigma\text{-}{}^3\Pi$ show quite similar variations as the case with resonant frequency (Fig. 4), a plateau gradually appears and becomes broad. Surprisingly, when I_0 reaches 4×10^{14} W/cm 2 , the angular distribution function in the ${}^3\Sigma\text{-}{}^3\Pi$ model forms a significant peak around $\beta = 0.1\pi$, sufficiently exceeding the plateau level, while for the case of negative detuning this effect is absent (see Fig. 7). This striking spectral difference between the positive and negative detunings can be explained by the interaction with a much larger density of rovibrational states above the resonance with the excited potential energy curve as compared to excitation below the resonance. Indeed, for the negative detuning, effectively, the intensity hitting the rovibrational states on the excited PES is smaller, so it resembles the low intensity case. Due to this, the spectral profiles computed including $\mathbf{R}\text{-}\Omega$ coupling for the negative detuning show less sensitivity to increasing the field intensity, and only the use of the highest intensity 4×10^{14} W/cm 2 allows us to see a sufficient effect of $\mathbf{R}\text{-}\Omega$ coupling around $\beta = 0.5\pi$. The observed complex dynamics behavior is related directly to different phases of rotational states triggered by the pulses, as explained below.

The fragment angular distribution computed for separate initial rotational states including $\mathbf{R}\text{-}\Omega$ coupling are presented in Fig. 8 for the case of positive (left panels) and negative (right panels) detuning from the resonance. For the relatively weak field $I_0 = 10^{13}$ W/cm 2 the angular distribution shows a quite similar profile as compared to the case of resonant pump field. However, as it clearly shows for the strong pump $I_0 = 4 \times 10^{14}$ W/cm 2 , all spectra originating from the degenerate initial states are sufficiently different from that of the resonant case (Fig. 5). In the case of negatively detuned pulses, peaks of spectra from different initial state $|J_0^w, M_0, \Omega_0\rangle$ narrow down and evolve toward $\beta = \pi/2$, but their relative intensities do not change too much and their averaged spectra show minor

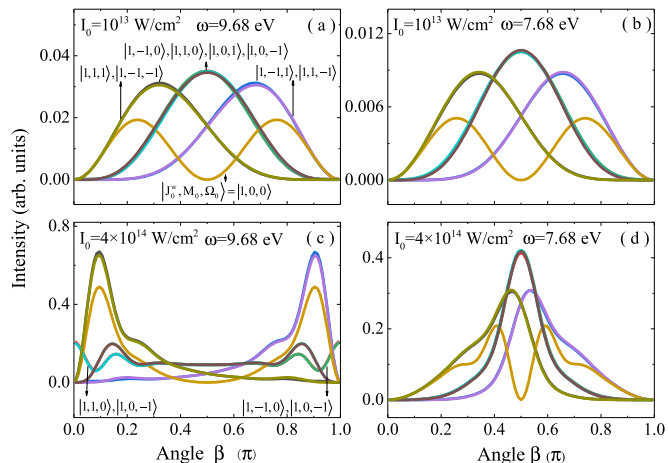


FIG. 8. Angular distribution of a different initial angular state (as in Fig. 5) but for positive (left panels (a, c)) and negative (right panels (b, d)) detuning and for two different pulse intensities $I_0 = 10^{13}$ W/cm 2 (a, b) and 4×10^{14} W/cm 2 (c, d).

changes. While in the case of positive detuning, contributions from initial rotational states $|1, 0, 0\rangle$, $|1, -1, -1\rangle$, $|1, 1, 1\rangle$, $|1, -1, 1\rangle$, and $|1, 1, -1\rangle$ increase their relative intensities, and their contributed peaks in the forward (or backward) region shift significantly to the small (or big) angle region with the increasing of I_0 (similar as that of the resonant case revealed in Fig. 5); furthermore, the peaks around $\pi/2$ from initial rotational states ($|1, -1, 0\rangle$, $|1, 1, 0\rangle$, $|1, 0, 1\rangle$ and $|1, 0, -1\rangle$) are strongly suppressed and new peaks appear at both small and big angle regions. The shifted and new arising peaks jointly contribute to the peak in the small angle region shown in Fig. 6.

Careful analysis of the amplitudes and phases for different rotational states reveals that the different rotational dynamics in the dissociative state is related to the phases created by the pump pulses. Moreover, these phases depend on the energy detuning from the resonance in the strong field case, when the $\mathbf{R}\text{-}\Omega$ coupling becomes important and results in different rotational excitations and, in turn, affects the relative phases between these states. So, in the case of strong field tuned from the resonance both phase effects and $\mathbf{R}\text{-}\Omega$ coupling affect the observable spectra. To illustrate this, let us consider an example when the initial rotational state $|1, 0, 0\rangle$ is promoted by the pump pulse to the ${}^3\Pi$ dissociative state. The main rotational contribution in this case is given by two rotational states $|2, 0, 1\rangle$ and $|4, 0, 1\rangle$, forming a rotational wave packet $c_1(|2, 0, 1\rangle + c_2|4, 0, 1\rangle)$, where coefficients c_1 and c_2 depend on the field intensity and detuning. When c_2 is real there is no phase difference between the rotational states, as it happens in the case of zero detuning. However, when there is a phase difference, as in the case of nonzero detuning, the c_2 coefficient becomes complex. Indeed, our numerical fitting of the angular distribution profiles in Figs. 8(c) and 8(d) results in the following approximated forms of the excited rotational wave packet $||2, 0, 1\rangle + e^{i0.2\pi}|4, 0, 1\rangle|^2$ and $||2, 0, 1\rangle + e^{i0.8\pi}|4, 0, 1\rangle|^2$, respectively. This example shows clearly the two opposite phases corresponding to the two opposite values of the detunings. In a similar way, considering

initial rotational states $|1, 0, -1\rangle$ and $|1, 1, 0\rangle$ (or $|1, 0, -1\rangle$ and $|1, -1, 0\rangle$) results in a significant fragmentation value at $\beta = 0$ (or π) when $I_0 = 4 \times 10^{14}$ W/cm² in the case of positive detuning, while these angles have almost zero intensity in the case of negative detuning. This shows that the energy detuning from the resonance can serve as a tool for fine control over phases of different rotational states and thus for the control of rotational dynamics in the photodissociation process.

IV. CONCLUSION

Unlike singlet state $^1\Sigma$ systems, the spin angular momentum also contributes to the electronic triplet state $^3\Sigma$, which triggers interest to understand the role of spin-orbital-rotation coupling or $\mathbf{R}\text{-}\Omega$ coupling in the photodissociation process pumped on the transition between $^3\Sigma$ and $^3\Pi$ states by intense pulses. As a showcase, photodissociation dynamics of the NH molecule from state $X^3\Sigma^-$ to $2^3\Pi$ by intense resonant and detuned VUV pulses have been comprehensively investigated using theoretical treatment accounting for the $\mathbf{R}\text{-}\Omega$ coupling. The two most important observable physical quantities, namely KER spectra and angular distribution of the fragments, are carefully studied for different pulse intensities and detuning from the resonance for nine degenerate initial angular states. It shows the final KER spectra are not very sensitive to the $\mathbf{R}\text{-}\Omega$ coupling, and due to the dressed potentials in the intense fields, the spectra will shift towards the lower and higher energy regions by intense negatively (and resonantly) and positively detuned pulses, respectively. The angular distributions are directly related to the rotational couplings, and the electron-rotation coupling keeps the angular distributed

photofragments always being a rising profile with respect to the angle β from 0 to $\pi/2$, while the initial rotational states $|1, 1, 0\rangle$ and $|1, 0, -1\rangle$ contribute the nonzero probabilities at $\beta = 0$. Furthermore, the probabilities in the small angles gradually increase as the increasing of the resonant and positively detuned pulse intensities, mainly contributed from the initial rotational states $|1, 1, 1\rangle$, $|1, -1, -1\rangle$, and $|1, 0, 0\rangle$. At the high pump intensity the angular distribution is found to be very sensitive to the detuning from the resonance, providing a new possibility for the fine control of photodissociation rotational dynamics.

As a perspective, the $\mathbf{R}\text{-}\Omega$ coupling is naturally there in states of diatomics with nonzero Ω , the present and previous work have shown its important effects in strong pulse excitation and dissociation, we would expect it would also play a role in the strong laser photoionization of diatomics, since at least one Ω of the neutral and ion must be nonzero (e.g., Ω of both O_2 and O_2^+ are nonzero), resulting into the participant of $\mathbf{R}\text{-}\Omega$ coupling in the nuclear dynamics. Further investigations in strong pulses are highly required to reveal the potential effect of $\mathbf{R}\text{-}\Omega$ coupling in different dynamics as in photoionization, photoabsorption, and so on.

ACKNOWLEDGMENTS

Grants from NSFC (No. 11934004, No. 11534011, and No. 11974230), the National Basic Research Program of China (2017YFA0403200), the Science Challenge Program of China (TZ2018005 and TZ2016005) are acknowledged. V.K. acknowledges financial support from Swedish Research Council (VR2019-03470) and the Ministry of Science and High Education of Russian Federation, Project No. FSRZ-2020-0008.

-
- [1] D. Strickland and G. Mourou, Compression of amplified chirped optical pulses, *Opt. Commun.* **56**, 219 (1985).
 - [2] T. Brabec and F. Krausz, Intense few-cycle laser fields: Frontiers of nonlinear optics, *Rev. Mod. Phys.* **72**, 545 (2000).
 - [3] F. Krausz and M. Ivanov, Attosecond physics, *Rev. Mod. Phys.* **81**, 163 (2009).
 - [4] P. B. Corkum, Plasma Perspective on Strong Field Multiphoton Ionization, *Phys. Rev. Lett.* **71**, 1994 (1993).
 - [5] K. J. Schafer, B. Yang, L. F. DiMauro, and K. C. Kulander, Above Threshold Ionization Beyond the High Harmonic Cutoff, *Phys. Rev. Lett.* **70**, 1599 (1993).
 - [6] S. Kim, J. Jin, Y.-J. Kim, I.-Y. Park, Y. Kim, and S.-W. Kim, High-harmonic generation by resonant plasmon field enhancement, *Nature (London)* **453**, 757 (2008).
 - [7] H. J. Wörner, J. B. Bertrand, D. V. Kartashov, P. B. Corkum, and D. M. Villeneuve, Following a chemical reaction using high-harmonic interferometry, *Nature (London)* **466**, 604 (2010).
 - [8] P. Emma, R. Akre, J. Arthur, R. Bionta, C. Bostedt *et al.*, First lasing and operation of an ångstrom-wavelength free-electron laser, *Nat. Photonics.* **4**, 641 (2010).
 - [9] J. Ullrich, A. Rudenko, and R. Moshhammer, Free-electron lasers: New avenues in molecular physics and photochemistry, *Annu. Rev. Phys. Chem.* **63**, 635 (2012).
 - [10] M. Harmand, R. Coffee, M. R. Bionta, M. Chollet, D. French *et al.*, Achieving few-femtosecond time-sorting at hard x-ray free-electron lasers, *Nat. Photonics.* **7**, 215 (2013).
 - [11] C. Bostedt, S. Boutet, D. M. Fritz, Z. Huang, H. J. Lee *et al.*, Linac coherent light source: The first five years, *Rev. Mod. Phys.* **88**, 015007 (2016).
 - [12] C. Pellegrini, A. Marinelli, and S. Reiche, The physics of x-ray free-electron lasers, *Rev. Mod. Phys.* **88**, 015006 (2016).
 - [13] J. H. Posthumus, The dynamics of small molecules in intense laser fields, *Rep. Prog. Phys.* **67**, 623 (2004).
 - [14] P. B. Corkum and F. Krausz, Attosecond science, *Nat. Phys.* **3**, 381 (2007).
 - [15] K. W. Ledingham, P. McKenna, and R. P. Singhal, Applications for nuclear phenomena generated by ultra-intense lasers, *Science* **300**, 1107 (2003).
 - [16] H. Stapelfeldt and T. Seideman, Colloquium: Aligning molecules with strong laser pulses, *Rev. Mod. Phys.* **75**, 543 (2003).
 - [17] M. Spanner, S. Patchkovskii, E. Frumker, and P. Corkum, Mechanisms of Two-Color Laser-Induced Field-Free Molecular Orientation, *Phys. Rev. Lett.* **109**, 113001 (2012).
 - [18] K. Lin, I. Tutunnikov, J. Qiang, J. Ma, Q. Song *et al.*, All-optical field-free three-dimensional orientation of asymmetric-top molecules, *Nat. Commun.* **9**, 5134 (2018).

- [19] A. S. Chatterley, C. Schouder, L. Christiansen *et al.*, Long-lasting field-free alignment of large molecules inside helium nanodroplets, *Nat. Commun.* **10**, 133 (2019).
- [20] E. Goulielmakis, Z.-H. Loh, A. Wirth, R. Santra, N. Rohringer *et al.*, Real-time observation of valence electron motion, *Nature (London)* **466**, 739 (2010).
- [21] C. Brif, R. Chakrabarti, and H. Rabitz, Control of quantum phenomena: Past, present and future, *New J. Phys.* **12**, 075008 (2010).
- [22] N. Berrah, L. Fang, B. Murphy, T. Osipov, K. Ueda *et al.*, Double-core-hole spectroscopy for chemical analysis with an intense x-ray femtosecond laser, *Proc. Natl. Acad. Sci.* **108**, 16912 (2011).
- [23] N. Rohringer, D. Ryan, R. A. London, M. Purvis, F. Albert *et al.*, Atomic inner-shell x-ray laser at 1.46 nanometres pumped by an x-ray free-electron laser, *Nature (London)* **481**, 488 (2012).
- [24] S. Chatterjee and T. Nakajima, Manipulation of resonant Auger processes using a strong bichromatic field, *Phys. Rev. A* **91**, 043413 (2015).
- [25] S. B. Zhang, V. Kimberg, and N. Rohringer, Nonlinear resonant Auger spectroscopy in CO using an x-ray pump-control scheme, *Phys. Rev. A* **94**, 063413 (2016).
- [26] O. Gessner and M. Gühr, Monitoring ultrafast chemical dynamics by time-domain x-ray photo- and Auger-electron spectroscopy, *Acc. Chem. Res.* **49**, 138 (2016).
- [27] D. Iablonskyi, K. Ueda, K. L. Ishikawa, A. S. Kheifets, P. Carpeggiani *et al.*, Observation and Control of Laser-Enabled Auger Decay, *Phys. Rev. Lett.* **119**, 073203 (2017).
- [28] P. H. Bucksbaum, A. Zavriyev, H. G. Muller, and D. W. Schumacher, Softening of the H_2^+ Molecular Bond in Intense Laser Fields, *Phys. Rev. Lett.* **64**, 1883 (1990).
- [29] A. Zavriyev, P. H. Bucksbaum, H. G. Muller, and D. W. Schumacher, Ionization and dissociation of H_2 in intense laser fields at 1.064 μm , 532 nm, and 355 nm, *Phys. Rev. A* **42**, 5500 (1990).
- [30] E. E. Aubanel, J.-M. Gauthier, and A. D. Bandrauk, Molecular stabilization and angular distribution in photodissociation of H_2^+ in intense laser fields, *Phys. Rev. A* **48**, 2145 (1993).
- [31] R. Numico, A. Keller, and O. Atabek, Laser-induced molecular alignment in dissociation dynamics, *Phys. Rev. A* **52**, 1298 (1995).
- [32] C. Wunderlich, E. Kobler, H. Figger, and T. W. Hänsch, Light-Induced Molecular Potentials, *Phys. Rev. Lett.* **78**, 2333 (1997).
- [33] K. Sändig, H. Figger, and T. W. Hänsch, Dissociation Dynamics of H_2^+ in Intense Laser Fields: Investigation of Photofragments from Single Vibrational Levels, *Phys. Rev. Lett.* **85**, 4876 (2000).
- [34] A. Csehi, G. J. Halász, L. S. Cederbaum, and A. Vibók, Competition between light-induced and intrinsic nonadiabatic phenomena in diatomics, *J. Phys. Chem. Lett.* **8**, 1624 (2017).
- [35] W. Zhang, X. Gong, H. Li *et al.*, Electron-nuclear correlated multiphoton-route to Rydberg fragments of molecules, *Nat. Commun.* **10**, 757 (2019).
- [36] P. Lu, J. Wang, H. Li *et al.*, High-order above-threshold dissociation of molecules, *Proc. Natl. Acad. Sci.* **115**, 2049 (2018).
- [37] X. Sun, M. Li, Y. Shao *et al.*, Vibrationally resolved electron-nuclear energy sharing in above-threshold multiphoton dissociation of CO, *Phys. Rev. A* **94**, 013425 (2016).
- [38] W. Zhang, Z. Yu, X. Gong *et al.*, Visualizing and Steering Dissociative Frustrated Double Ionization of Hydrogen Molecules, *Phys. Rev. Lett.* **119**, 253202 (2017).
- [39] G. J. Halász, A. Vibók, N. Moiseyev, and L. S. Cederbaum, Nuclear-wave-packet quantum interference in the intense laser dissociation of the D_2^+ molecule, *Phys. Rev. A* **88**, 043413 (2013).
- [40] A. Csehi, G. J. Halász, L. S. Cederbaum, and A. Vibók, Tracking the photodissociation probability of D_2^+ induced by linearly chirped laser pulses, *J. Chem. Phys.* **144**, 074309 (2016).
- [41] A. Csehi, G. J. Halász, L. S. Cederbaum, and A. Vibók, Photodissociation of D_2^+ induced by linearly chirped laser pulses, *J. Chem. Phys.* **143**, 014305 (2015).
- [42] A. Tóth, A. Csehi, G. J. Halász, and A. Vibók, Control of photodissociation with the dynamic Stark effect induced by THz pulses, *Phys. Rev. Res.* **2**, 013338 (2020).
- [43] A. Tóth, A. Csehi, G. J. Halász, and A. Vibók, Photodissociation dynamics of the LiF molecule: Two- and three-state descriptions, *Phys. Rev. A* **99**, 043424 (2019).
- [44] A. Tóth, P. Badankó, G. J. Halász, A. Vibók, and A. Csehi, Importance of the lowest-lying electronic state in the photodissociation dynamics of LiF, *Chem. Phys.* **515**, 418 (2018).
- [45] P. Badankó, G. J. Halász, L. S. Cederbaum, A. Vibók, and A. Csehi, Communication: Substantial impact of the orientation of transition dipole moments on the dynamics of diatomics in laser fields, *J. Chem. Phys.* **149**, 181101 (2018).
- [46] T. Szidarovszky, G. J. Halász, A. G. Császár, L. S. Cederbaum, and A. Vibók, Direct signatures of light-induced conical intersections on the field-dressed spectrum of Na_2 , *J. Phys. Chem. Lett.* **9**, 2739 (2018).
- [47] A. Csehi, G. J. Halász, and A. Vibók, Collective effect of light-induced and natural nonadiabatic phenomena in the dissociation dynamics of the NaI molecule, *Chem. Phys.* **509**, 91 (2018).
- [48] Y.-C. Han, K.-J. Yuan, W.-H. Hu, and S.-L. Cong, Control of photodissociation and photoionization of the NaI molecule by dynamic Stark effect, *J. Chem. Phys.* **130**, 044308 (2009).
- [49] Z.-Y. Zhao, Y.-C. Han, J. Yu, and S.-L. Cong, The influence of field-free orientation on the predissociation dynamics of the NaI molecule, *J. Chem. Phys.* **140**, 044316 (2014).
- [50] Y. R. Liu, Y. Wu, J. G. Wang, O. Vendrell, V. Kimberg, and S. B. Zhang, Electron-rotation coupling in diatomics under strong-field excitation, *Phys. Rev. A* **102**, 033114 (2020).
- [51] R. N. Zare, *Angular Momentum: Understanding Spatial Aspects in Chemistry and Physics* (John Wiley & Sons, New York, 1988).
- [52] M. Beck, A. Jackle, G. Worth, and H.-D. Meyer, The multiconfiguration time-dependent Hartree (MCTDH) method: A highly efficient algorithm for propagating wavepackets, *Phys. Rep.* **324**, 1 (2000).
- [53] H. Lefebvre-Brion and R. W. Field, *The Spectra and Dynamics of Diatomic Molecules: Revised and Enlarged Edition* (Elsevier, New York, 2004).

- [54] E. M. Goldfield and K. P. Kirby, *Ab initio* studies of low-lying $^3\Sigma^-$, $^3\Pi$, and $^5\Sigma^-$ states of NH. I. Potential curves and dipole moment functions, *J. Chem. Phys.* **87**, 3986 (1987).
- [55] G. A. Worth, M. H. Beck, A. Jäckle, O. Vendrell, and H.-D. Meyer, The MCTDH Package, Version 8.2, (2000). H.-D. Meyer, Version 8.3 (2002), Version 8.4 (2007). O. Vendrell and H.-D. Meyer Version 8.5 (2013). Version 8.5 contains the ML-MCTDH algorithm. Current versions: 8.4.18 and 8.5.11 (2019). Used version: exchange with “Used version.” See <http://mctdh.uni-hd.de/>.
- [56] P. V. Demekhin and L. S. Cederbaum, Dynamic Interference of Photoelectrons Produced by High-Frequency Laser Pulses, *Phys. Rev. Lett.* **108**, 253001 (2012).
- [57] S. B. Zhang and N. Rohringer, Photoemission spectroscopy with high-intensity short-wavelength lasers, *Phys. Rev. A* **89**, 013407 (2014).